ARTICLE

Inverse Heavy-Atom Effect in Near Infrared Photoluminescent Gold Nanoclusters

Goutam Pramanik,[a,e] Klaudia Kvakova,[a] Muhammed Arshad Thottappali,[b,c] David Rais,[b] Jiri Pfleger,[b] Michael Greben,[c] Ayman El-Zoka,[d] Sara Bals,[d] Martin Dracinsky,[a] Jan Valenta,[c,*] and Petr Cigler[a,*]

Fluorophores functionalized with heavy elements show enhanced intersystem crossing due to increased spin–orbit coupling, which in turn shortens the fluorescence decay lifetime (τ^{PL}). This phenomenon is known as the heavy-atom effect (HAE). Here, we report the observation of increased τ^{PL} upon functionalisation of near-infrared photoluminescent gold nanoclusters with iodine. The heavy atom-mediated increase in τ^{PL} is in striking contrast with the HAE and referred to as inverse HAE. Femtosecond and nanosecond transient absorption spectroscopy revealed overcompensation of a slight decrease in lifetime of the transition associated with the Au core (ps) by a large increase in the long-lived triplet state lifetime associated with Au shell, which contributed to the observed inverse HAE. This unique observation of inverse HAE in gold nanoclusters provides the means to enhance the triplet excited state lifetime.

1. Introduction

Triplet excited states are of great interest because their properties are suitable for a wide range of applications, including photochemical reactions,[1] photovoltaics,[2] photosensitizers[3] and organic light-emitting diodes[4]. Extended utilization of the triplet state energy enables high efficiency of energy conversion and limits heat dissipation.[5] Manipulation of triplet lifetimes can greatly alter the functionalities of nanomaterials. Triplet excited states are very rarely accessed by direct excitation, but can be readily populated through intersystem crossing (ISC). However, transitions between states with different spin multiplicities are forbidden by selection rules in the absence of spin-orbit coupling (SOC), and as a result, the rate of emission from triplets is several orders of magnitude smaller than that of fluorescence. One feasible strategy to achieve effective ISC is to introduce heavy atoms such as iodine into the fluorophores. The inclusion of heavy atoms in the molecular structure promotes SOC between the singlet and triplet states, which leads to more efficient ISC.[6] The influence of a substituent atom with large atomic number on molecular SOC is termed the heavy-atom effect (HAE). Heavy atom-induced enhanced SOC is accompanied by a reduction in triplet excited state lifetime.[7]

In the last two decades, photoluminescent gold nanoclusters (AuNCs) have emerged as a new class of material for sensing,[8,9] catalysis[10–13] and bioimaging[14–16] applications. Ultrasmall AuNCs containing only a few Au atoms, with size comparable to the de Broglie wavelength of electrons, display molecule-like interactions with incident light to produce intense photoluminescence (PL).[17–19] Their electronic and optical properties depend on the cluster core structure, surface capping ligands and surrounding environment.[20–38] However, in molecular-sized AuNCs, the majority of the Au atoms are located on the surface of the inorganic core, and therefore, the protecting ligands play an important role in modulating their properties.[20,27,39–41] For example, Jin and co-workers found that near infrared (NIR) emission depends on the electron donating capabilities of the ligand shell and proposed a mechanism for charge-transfer relaxation from the ligand shell to the metal core.[31] Murray and co-workers demonstrated enhancement of the PL intensity of gold nanoparticles with an increase in thiol ligand density.[40] Several other factors play a pivotal role in the PL properties of AuNCs. These include the functionality and nature of the coordinating ligand,[42,43] denticity,[44] polarization of the Au–S core-ligand interaction,[40,45] length of Au–S staple bonds,[22] ligand coordination numbers and ligand arrangements,[46] and rigidity of the ligand shell[24]. The HAE of gold influences both ground- and excited-state properties and opens access to triplet-state photophysics.[47] The surface Au(I)–S triplet state and ligand-to-metal charge transfer have been widely proposed as explanations for the NIR PL from AuNCs.[24,48]

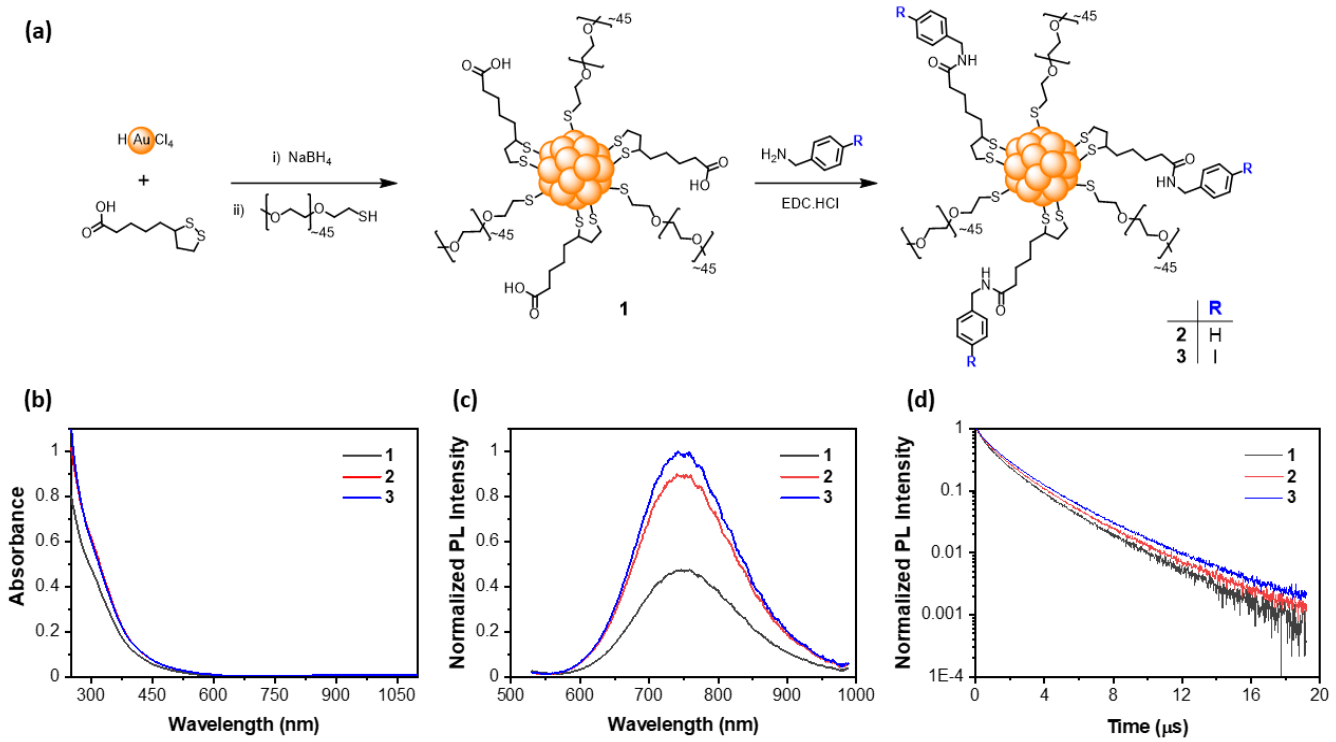

Figure 1: (a) Synthetic scheme leading to NIR PL AuNCs. EDC.HCl: *N*-(3-dimethylaminopropyl)-*N'*-ethylcarbodiimide hydrochloride. (b) Absorption spectra of 200 μg/mL aqueous solutions of AuNCs. (c) PL spectra of 200 μg/mL aqueous solutions of AuNCs upon excitation at 405 nm. (d) Normalized time-resolved PL decay curves of AuNCs at the peak of 740 nm (λ_{ex} 405 nm).

The strong dependence of the optical properties of AuNCs on surface capping ligands motivated us to explore the influence of heavy atoms in the ligand sphere on the optical properties of AuNCs. Here, we report the influence of an iodine functionalised ligand on the optical properties of NIR PL AuNCs. Interestingly, time-resolved PL spectroscopy and ultrafast transient absorption spectroscopy revealed that iodinated AuNCs exhibit increased PL lifetime and triplet excited state lifetime compared to the non-iodinated analogue. This anomalous inverse HAE contrasts sharply with classical HAE and is rarely observed.[49–51]

2. Results and Discussion

2.1. Synthesis and Characterisation of AuNCs

Our approach to synthesis of NIR PL AuNCs was guided by previous observations that ligands presenting more than one coordinating group provide improved colloidal stability to nanoclusters and that poly(ethylene glycol) (PEG) moieties promote excellent aqueous solubility.[44,52] An aqueous solution of bidentate thioctic acid and thiol-terminated PEG-protected NIR PL AuNCs (**1**, see **Fig. 1a**) was prepared and characterised according to a previously reported protocol.[53,54] To evaluate the dependence of optical properties on the presence of a heavy atom in the ligand sphere, **1** was conjugated with 4-iodobenzylamine *via* EDC-mediated amidic coupling with surface carboxyl groups to obtain **3** (Fig. 1a). The rationale behind the chosen ligand, 4-iodobenzylamine, lies in the stability of the aryl-iodide in aqueous solution and higher reactivity of activated O-acylisourea ester towards a primary amine compared to an aromatic amine. As a control, **2** was prepared by coupling **1** with benzylamine. The synthetic scheme of AuNCs is presented in **Fig. 1a**, and detailed synthetic procedures are described in the ESI.

To quantify the ratio of Au and attached ligand, a combined method of CHN analysis and inductively coupled plasma optical emission spectroscopy (ICP-OES) was performed. This analysis revealed that in both **2** and **3**, the molar Au/S ratio was ~1:0.7 and the Au/N ratio was ~4.2-4.3:1 (**Table S1** in ESI). The ligand stoichiometry and the degree of substitution by amines was therefore the same for both **2** and **3**.

We employed ^{1}H NMR spectroscopy to further analyse the chemical structure of the AuNCs. The ^{1}H NMR spectra of **2** and **3** (**Fig. S1** in ESI) show broad signals corresponding to the thioctic acid, PEG and benzyl moieties. This may be explained by interactions between the organic ligands and the paramagnetic species, leading to signal broadening due to paramagnetic relaxation enhancement. The signals of three non-equivalent aromatic protons of the benzylamine group in **2** overlap in a broad peak at 7.2 ppm, while two aromatic signals corresponding to two non-equivalent aromatic protons in **3** are clearly visible. Elemental analysis and ^{1}H NMR clearly indicated that the benzyl moiety was successfully coupled to **1**.

High resolution scanning transmission electron microscopy (HR-STEM) revealed non-aggregated AuNCs with average diameters of 1.40 ± 0.41 nm (**Fig. S2 a, b**) and 1.38 ± 0.39 nm (**Fig. S2 d, e**) for **2** and **3**, respectively. This observation ruled

out the possibility of aggregation-induced inverse HAE.[55] The average zeta potential values of **2** and **3** were -5.5 ± 0.3 and -5.3 ± 0.5 mV, respectively, in phosphate buffer (10 mM, pH 7.4). The negative zeta potential is likely due to negatively charged unreacted carboxylic groups on the surface of the AuNCs.

To determine the electronic states of gold in the AuNCs, we used the XPS technique. The binding energy (BE) of Au $4f_{7/2}$ of **2** and **3** (**Fig. S2 c, f**) falls between the energies of Au(0) (84 eV) and Au(I) (86 eV) of gold thiolate, suggesting the coexistence of Au(0) and Au(I) in both AuNCs.[56,57] The Au 4f component from Au–S bonds in AuNCs is positively shifted relative to that from Au–Au bonds due to charge transfer from the NC to the thiol.[58]

To more accurate determine of elemental composition of AuNCs, we employed electrospray ionization mass spectrometry (ESI MS), which has been previously used for analysis of AuNCs functionalized with small molecules.[22,59,60] However, our AuNCs showed no reasonable signal under different ionization conditions in both positive and negative modes. We hypothesize that presence of high molecular weight ligands (e. g., PEG) on AuNCs may attenuate ionization in ESI MS analysis.

2.2. Optical Properties of AuNCs

The AuNCs absorbed strongly in the ultraviolet range (< 400 nm), as evidenced by UV–vis absorption spectra (Fig. 1b). AuNCs **2** and **3** showed slightly higher absorption than **1**. As expected, due to their ultrasmall size, AuNCs do not possess a characteristic surface plasmon resonance absorption around 520 nm. An absorption around 680 nm attributable to the HOMO to LUMO transition for the Au_{25} cluster also was not observed.[61–64] AuNC **1** showed broad weak emission in the visible-to-NIR region with a maximum around 740 nm (**Fig. 1c**). On the basis of emission maxima in photoluminescence spectra (~740 nm) and average diameter of the Au core, the approximate number of atoms per NC is expected to be around ~ 25-32. Upon introduction of benzylamine moiety to the AuNCs, the PL intensity increased (**Fig. 1c**) with the emission maximum at ~740 nm remaining unaltered. The enhancement of PL can be attributed to the electron donating capability of the benzyl group.[31] Interestingly, **3** showed slightly higher PL intensity than **2**, even though these AuNCs contain a similar number of conjugated 4-iodobenzylamine and benzylamine moieties. The PL quantum yields of **2** and **3** were ~11% and 15%, respectively (**Fig. S3** in ESI). The higher PL of **3** can likely be attributed to the electron-rich iodine facilitating enhanced radiative decay from the triplet excited state.

The PL decay of AuNCs in aqueous solution was determined upon excitation at 405 nm (5-µs pulses of rectangular shape). The time-resolved PL decay profiles of AuNCs are shown in **Fig. 1d**. The AuNCs exhibited long excited state lifetimes (>100 ns). PL decay kinetics fitting of **2** and **3** at the PL peak (740 nm) required three exponentials for a perfect fit (R^2 > 0.9999). All three components were significant but have no direct physical meaning, as a three-exponential decay can fit almost any decay curve and could also indicate a continuous distribution of lifetimes.[65] **Table 1** lists the individual components extracted from the fits for **2** and **3**. Notably, upon iodination, the amplitude of the fast decaying components (A_1, A_2) decreased, whereas the amplitude of the slowest decaying component (A_3) increased. Such long life-time components (>100 ns) are characteristic of Au(I)–thiol complexes, and observation of long PL decay in AuNCs suggests that such complexes contribute to the luminescence of AuNCs.[66] The pronounced long lifetimes for NIR PL can be attributed to the gold shell states [Au(I)–S] in which significant ligand contribution is present.[31,67,68] Interestingly, iodine-functionalised AuNC **3** had a slower PL decay compared to **2**, and the amplitude average PL lifetime increased from 1.64 µs (**2**) to 1.75 µs (**3**). As both AuNCs (**2, 3**) have similar core, zeta potential, number of ligands, and chemical structure, the increase in PL lifetime in **3** compared to **2** can be attributed to the presence of the heavy atom iodine in the ligand sphere.

Table 1. The amplitudes of three lifetime components of the PL decay (Fig. 1d) for **2** and **3** in air-saturated solution fitted with a three-exponential function. The corresponding relative amplitude (A_i) for each τ_i^{PL} is indicated in parentheses.

Set of τ^{PL} used for the fit	τ_1^{PL} (0.4 µs)	τ_2^{PL} (1.5 µs)	τ_3^{PL} (3.6 µs)
	A_1	A_2	A_3
2	0.26	0.57	0.20
3	0.24	0.55	0.26

Typically, with addition of heavy atoms to a fluorophore, the greater SOC due to HAE gives rise to faster ISC and triplet radiative decay ($T_1 \rightarrow S_0$). Substitution of hydrogen atoms with heavy atoms such as iodine typically results in shorter lifetimes and lower quantum yields.[69] Thus, our observation of longer PL lifetime and higher quantum yield upon addition of the heavy atom iodine is surprising.

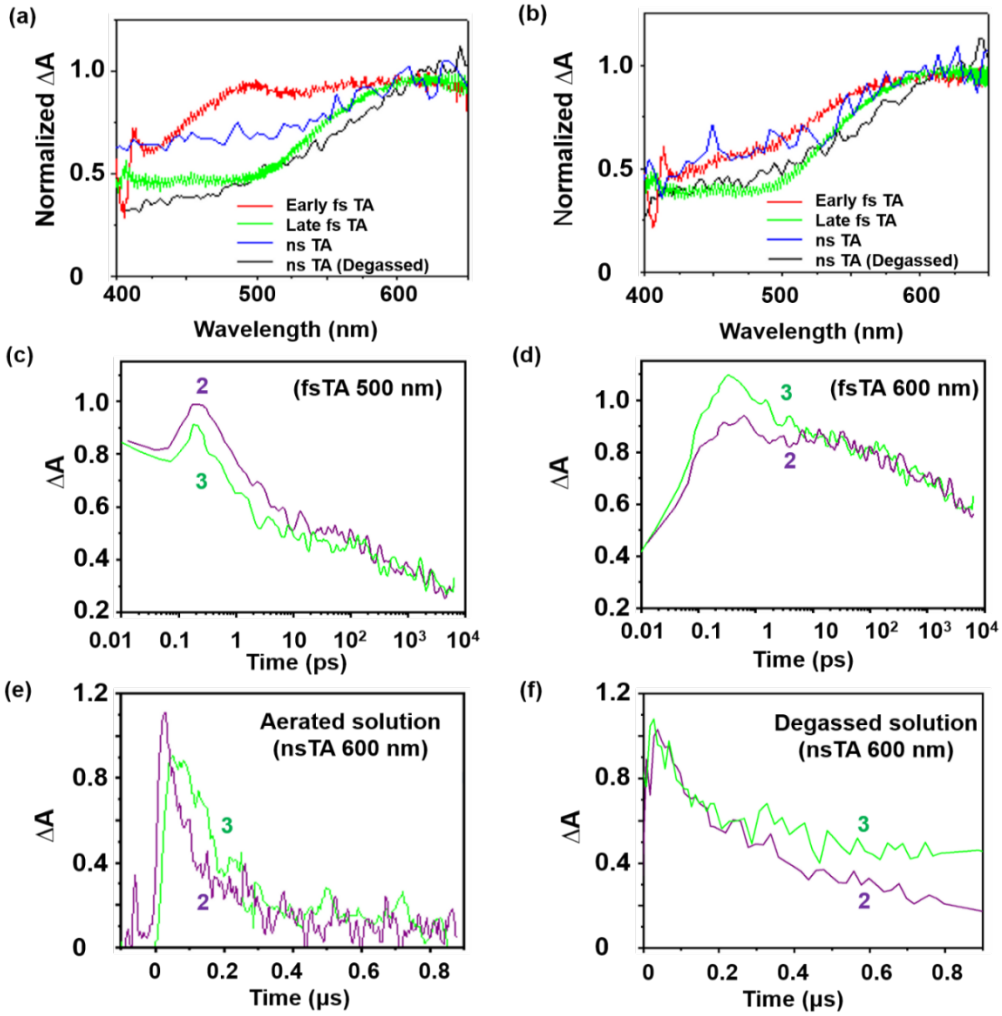

Figure 2. Transient absorption spectra of colloidal solutions **2** (a) and **3** (b). Normalized kinetic traces obtained from the femtosecond transient absorption (fsTA) signal at probe wavelengths of 500 nm (c) and 600 nm (d). Normalized kinetic traces obtained from the nanosecond transient absorption (nsTA) signal at the 600 nm probe wavelength of aerated aqueous solution (e) and degassed aqueous solution of AuNCs (f). Excitation wavelength were 360 nm (fsTA) and 355 nm (nsTA).

2.3. Excited State Dynamics of the AuNCs

To understand this apparent inverse HAE, we analysed aqueous colloidal solutions of **2** and **3** by transient absorption spectroscopy. Femtosecond transient absorption (fsTA) and nanosecond transient absorption (nsTA) spectroscopy were used to gain insight into the excited state dynamics of AuNCs covering the picosecond and nanosecond time scale. A broad positive signal in the range of 400-650 nm indicates that the transient signal originates solely from excited-state absorption (ESA) (**Fig. 2a, b**). Excited state absorption–time profiles recorded at probe wavelengths 500 and 600 nm are shown in **Fig. 2c, d**. The transient absorption spectral profiles of both AuNCs were quite similar, with two distinguishable transient features: an ultrafast decay characterised with a time constant τ_1^{TA} and a long-lived excited state decay with a time constant τ_2^{TA}. The transient spectrum of fast decaying species of **2** showed more pronounced absorption band centred at 490 nm. When fitting the nsTA experimental data by a more appropriate bi-exponential decay, an additional component was found, with a life time τ_3^{TA} >> 10 μs, much exceeding the time scale of the experimental setup (see Figs. **S4—S5** and the respective section in the ESI for further details). The presence of excited states with two lifetimes is consistent with reported characteristics of AuNC excited states.[61,62,70–72] The quenching of the long lived excited states by dissolved oxygen (τ_2^{TA}, **Table 2**) evidences their triplet nature. This long-lived excited state is responsible for the intense NIR emission in AuNCs.[22,62,63,70,72] Based on previous reports[24,61] and our experimental results, we assigned the fast relaxation (τ_1^{TA}) to core–shell relaxation or electronic rearrangement within the AuNC core, which then undergoes ISC to populate the triplet states of the shell gold.[24] The triplet excited state then decays to the ground state (**Fig. 3**). The fast component of the transient absorption decay was approximated by an exponential kinetics with lifetimes τ_1^{TA} of 3.78 ± 0.01 and 3.16 ± 0.07 ps for **2** and **3**, respectively (**Table 2**).

Table 2: Lifetimes derived from individual spectral components.

Sample	fsTA τ_1^{TA} (ps)	nsTA, air-saturated τ_2^{TA} (µs)	nsTA, degassed τ_3^{TA} (µs)
2	3.78 ± 0.01	0.07 ± 0.01	0.28 ± 0.01
3	3.16 ± 0.07	0.13 ± 0.01	1.86 ± 0.03

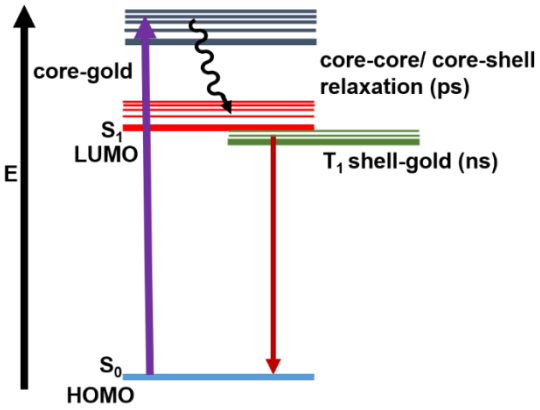

Figure 3: Proposed scheme of photoexcitation and relaxation pathways of NIR PL AuNCs.

In the presence of dissolved oxygen, the corresponding long lifetime excited state had lifetimes τ_2^{TA} of 70 ± 2 and 130 ± 10 ns for **2** and **3**, respectively. In a degassed aqueous environment, iodination increased the triplet state lifetime τ_2^{TA} by ~6.6-fold (0.28 µs to 1.86 µs). It is evident that iodination of AuNCs accelerates the core−shell relaxation or electronic rearrangement within the core and decelerates the relaxation from the triplet state to the ground state. The prolonged lifetime of the excited triplet state indicates suppression of its non-radiative deactivation in favour of radiative decay.

Overall, our data suggest an inverse HAE (i.e., enhanced PL quantum yield and longer decay) for iodine-functionalised **3**. The acceleration of the decay of the excited state to the ground state at nanosecond timescale in an absence of iodine indicates a presence of an additional parallel quenching process in the sample **2**. We hypothesize that this process is responsible for quenching of PL. In the presence of ligand with iodine this quenching process is suppressed, supporting thus the radiative channel.

3. Conclusions

Based on the combined optical analyses of steady state, time resolved, femtosecond and nanosecond transient absorption, we demonstrated inverse HAE in thioctic acid- and PEG-stabilized NIR PL AuNCs. The observation of inverse HAE came as a surprise, as it is very rare. However, the discovery of inverse HAE in AuNCs provides an excellent route to enhance the long-lived triplet excited lifetime. Moreover, enhanced triplet state lifetime *via* inverse HAE could provide a design principle for AuNC-based triplet photosensitizers, photocatalysts and other applications because the intermolecular electron transfer or energy transfer are more efficient with longer triplet state lifetimes. Iodine and other heavy elements may be further explored in future work for tuning of exciton lifetime of the PL metal clusters. The findings demonstrate that surface ligand interactions with the Au core play a critical role in dictating the optical properties of the nanocluster.

Conflicts of interest

There are no conflicts to declare.

Acknowledgements

The authors acknowledge support from GACR project Nr.18-12533S. G. P. acknowledges support from EUSMI project No. E180200060; J.P. from the Ministry of Education, Youth and Sports of the Czech Republic - Program INTER-EXCELLENCE (LTAUSA19066).

References

1 J. Zhao, W. Wu, J. Sun and S. Guo, *Chem. Soc. Rev.*, 2013, **42**, 5323–5351.
2 W.-Y. Wong and C.-L. Ho, *Acc. Chem. Res.*, 2010, **43**, 1246–1256.
3 Y. Hou, Q. Liu and J. Zhao, *Chem. Commun.*, 2020, **56**, 1721–1724.
4 M. J. Walter and J. M. Lupton, in *Highly Efficient OLEDs with Phosphorescent Materials*, John Wiley & Sons, Ltd, 2008, pp. 99–129.
5 J. Wang, X. Gu, H. Ma, Q. Peng, X. Huang, X. Zheng, S. H. P. Sung, G. Shan, J. W. Y. Lam, Z. Shuai and B. Z. Tang, *Nat. Commun.*, 2018, **9**, 2963.
6 A. Rodriguez-Serrano, V. Rai-Constapel, M. C. Daza, M. Doerr and C. M. Marian, *Phys. Chem. Chem. Phys.*, 2015, **17**, 11350–11358.
7 O. Elbjeirami, M. A. Rawashdeh-Omary and M. A. Omary, *Res. Chem. Intermed.*, 2011, **37**, 691.
8 L.-Y. Chen, C.-W. Wang, Z. Yuan and H.-T. Chang, *Anal. Chem.*, 2015, **87**, 216–229.
9 Y. Xiao, Z. Wu, Q. Yao and J. Xie, *Aggregate*, 2021, **2**, 114–132.
10 R. Jin, C. Zeng, M. Zhou and Y. Chen, *Chem. Rev.*, 2016, **116**, 10346–10413.
11 Z. Liu, Z. Wu, Q. Yao, Y. Cao, O. J. H. Chai and J. Xie, *Nano Today*, 2021, **36**, 101053.
12 S. Tian, Y. Cao, T. Chen, S. Zang and J. Xie, *Chem. Commun.*, 2020, **56**, 1163–1174.
13 O. J. H. Chai, Z. Liu, T. Chen and J. Xie, *Nanoscale*, 2019, **11**, 20437–20448.
14 H. Liu, G. Hong, Z. Luo, J. Chen, J. Chang, M. Gong, H. He, J. Yang, X. Yuan, L. Li, X. Mu, J. Wang, W. Mi, J. Luo, J. Xie and X.-D. Zhang, *Adv. Mater.*, 2019, **31**, 1901015.
15 Y. G. Srinivasulu, Q. Yao, N. Goswami and J. Xie, *Mater. Horiz.*, 2020, **7**, 2596–2618.
16 I. Chakraborty and T. Pradeep, *Chem. Rev.*, 2017, **117**, 8208–8271.

17 T. P. Bigioni, R. L. Whetten and Ö. Dag, *J. Phys. Chem. B*, 2000, **104**, 6983–6986.
18 J. Zheng, J. T. Petty and R. M. Dickson, *J. Am. Chem. Soc.*, 2003, **125**, 7780–7781.
19 S. Link, A. Beeby, S. FitzGerald, M. A. El-Sayed, T. G. Schaaff and R. L. Whetten, *J. Phys. Chem. B*, 2002, **106**, 3410–3415.
20 D. M. Chevrier, L. Raich, C. Rovira, A. Das, Z. Luo, Q. Yao, A. Chatt, J. Xie, R. Jin, J. Akola and P. Zhang, *J. Am. Chem. Soc.*, 2018, **140**, 15430–15436.
21 Z. Luo, X. Yuan, Y. Yu, Q. Zhang, D. T. Leong, J. Y. Lee and J. Xie, *J. Am. Chem. Soc.*, 2012, **134**, 16662–16670.
22 Y. Yu, Z. Luo, D. M. Chevrier, D. T. Leong, P. Zhang, D. Jiang and J. Xie, *J. Am. Chem. Soc.*, 2014, **136**, 1246–1249.
23 A. Mathew, E. Varghese, S. Choudhury, S. K. Pal and T. Pradeep, *Nanoscale*, 2015, **7**, 14305–14315.
24 K. Pyo, V. D. Thanthirige, K. Kwak, P. Pandurangan, G. Ramakrishna and D. Lee, *J. Am. Chem. Soc.*, 2015, **137**, 8244–8250.
25 M. Sugiuchi, Y. Shichibu, T. Nakanishi, Y. Hasegawa and K. Konishi, *Chem. Commun.*, 2015, **51**, 13519–13522.
26 M. Iwasaki, N. Kobayashi, Y. Shichibu and K. Konishi, *Phys. Chem. Chem. Phys.*, 2016, **18**, 19433–19439.
27 K. Konishi, M. Iwasaki, M. Sugiuchi and Y. Shichibu, *J. Phys. Chem. Lett.*, 2016, **7**, 4267–4274.
28 N. Goswami, Q. Yao, Z. Luo, J. Li, T. Chen and J. Xie, *J. Phys. Chem. Lett.*, 2016, **7**, 962–975.
29 T. Yang, S. Dai, S. Yang, L. Chen, P. Liu, K. Dong, J. Zhou, Y. Chen, H. Pan, S. Zhang, J. Chen, K. Zhang, P. Wu and J. Xu, *J. Phys. Chem. Lett.*, 2017, **8**, 3980–3985.
30 J. Zheng, C. Zhang and R. M. Dickson, *Phys. Rev. Lett.*, 2004, **93**, 077402.
31 Z. Wu and R. Jin, *Nano Lett.*, 2010, **10**, 2568–2573.
32 M. Zhou, T. Higaki, Y. Li, C. Zeng, Q. Li, M. Y. Sfeir and R. Jin, *J. Am. Chem. Soc.*, 2019, **141**, 19754–19764.
33 M. Zhou, T. Higaki, G. Hu, M. Y. Sfeir, Y. Chen, D. Jiang and R. Jin, *Science*, 2019, **364**, 279–282.
34 S. Wang, X. Meng, A. Das, T. Li, Y. Song, T. Cao, X. Zhu, M. Zhu and R. Jin, *Angew. Chem. Int. Ed.*, 2014, **53**, 2376–2380.
35 C. Yao, C.-Q. Xu, I.-H. Park, M. Zhao, Z. Zhu, J. Li, X. Hai, H. Fang, Y. Zhang, G. Macam, J. Teng, L. Li, Q.-H. Xu, F.-C. Chuang, J. Lu, C. Su, J. Li and J. Lu, *Angew. Chem.*, 2020, **132**, 8347–8353.
36 Q. Li, M. Zhou, W. Y. So, J. Huang, M. Li, D. R. Kauffman, M. Cotlet, T. Higaki, L. A. Peteanu, Z. Shao and R. Jin, *J. Am. Chem. Soc.*, 2019, **141**, 5314–5325.
37 Z. Wu, Q. Yao, O. J. H. Chai, N. Ding, W. Xu, S. Zang and J. Xie, *Angew. Chem.*, 2020, **132**, 10020–10025.
38 T. Higaki, C. Liu, C. Zeng, R. Jin, Y. Chen, N. L. Rosi and R. Jin, *Angew. Chem. Int. Ed.*, 2016, **55**, 6694–6697.
39 P. Charchar, A. J. Christofferson, N. Todorova and I. Yarovsky, *Small*, 2016, **12**, 2395–2418.
40 G. Wang, R. Guo, G. Kalyuzhny, J.-P. Choi and R. W. Murray, *J. Phys. Chem. B*, 2006, **110**, 20282–20289.
41 A. Tlahuice-Flores, R. L. Whetten and M. Jose-Yacaman, *J. Phys. Chem. C*, 2013, **117**, 20867–20875.
42 S. E. Crawford, C. M. Andolina, A. M. Smith, L. E. Marbella, K. A. Johnston, P. J. Straney, M. J. Hartmann and J. E. Millstone, *J. Am. Chem. Soc.*, 2015, **137**, 14423–14429.
43 Z. Lei, X.-K. Wan, S.-F. Yuan, J.-Q. Wang and Q.-M. Wang, *Dalton Trans.*, 2017, **46**, 3427–3434.
44 F. Aldeek, M. A. H. Muhammed, G. Palui, N. Zhan and H. Mattoussi, *ACS Nano*, 2013, **7**, 2509–2521.
45 J. Jiang, C. V. Conroy, M. M. Kvetny, G. J. Lake, J. W. Padelford, T. Ahuja and G. Wang, *J. Phys. Chem. C*, 2014, **118**, 20680–20687.
46 J. Liu, P. N. Duchesne, M. Yu, X. Jiang, X. Ning, R. D. Vinluan, P. Zhang and J. Zheng, *Angew. Chem. Int. Ed.*, 2016, **55**, 8894–8898.
47 L. Gao, M. A. Peay, D. V. Partyka, J. B. Updegraff, T. S. Teets, A. J. Esswein, M. Zeller, A. D. Hunter and T. G. Gray, *Organometallics*, 2009, **28**, 5669–5681.
48 A. Cantelli, G. Guidetti, J. Manzi, V. Caponetti and M. Montalti, *Eur. J. Inorg. Chem.*, 2017, **2017**, 5068–5084.
49 J. H. Flanagan, Jr., S. E. Romero, B. L. Legendre, Jr., R. P. Hammer and S. A. Soper, in *Advances in Fluorescence Sensing Technology III*, International Society for Optics and Photonics, 1997, vol. 2980, pp. 328–337.
50 D. A. Head, A. Singh, M. G. Cook and M. J. Quinn, *Can. J. Chem.*, 1973, **51**, 1624–1633.
51 N. J. Turro, G. Kavarnos, V. Fung, A. L. Lyons and T. Cole, *J. Am. Chem. Soc.*, 1972, **94**, 1392–1394.
52 M. H. Stewart, K. Susumu, B. C. Mei, I. L. Medintz, J. B. Delehanty, J. B. Blanco-Canosa, P. E. Dawson and H. Mattoussi, *J. Am. Chem. Soc.*, 2010, **132**, 9804–9813.
53 G. Pramanik, A. Keprova, J. Valenta, V. Bocan, K. Kvaková, L. Libusova and P. Cigler, *J. Vis. Exp.*, 2020, **157**, e60388.
54 G. Pramanik, J. Humpolickova, J. Valenta, P. Kundu, S. Bals, P. Bour, M. Dracinsky and P. Cigler, *Nanoscale*, 2018, **10**, 3792–3798.
55 P. Xu, Q. Qiu, X. Ye, M. Wei, W. Xi, H. Feng and Z. Qian, *Chem. Commun.*, 2019, **55**, 14938–14941.
56 Y. Negishi, K. Nobusada and T. Tsukuda, *J. Am. Chem. Soc.*, 2005, **127**, 5261–5270.
57 C. Zhou, C. Sun, M. Yu, Y. Qin, J. Wang, M. Kim and J. Zheng, *J. Phys. Chem. C*, 2010, **114**, 7727–7732.
58 P. Zhang and T. K. Sham, *Phys. Rev. Lett.*, 2003, **90**, 245502.
59 T. Chen, Q. Yao, R. R. Nasaruddin and J. Xie, *Angew. Chem. Int. Ed.*, 2019, **58**, 11967–11977.
60 X. Yuan, B. Zhang, Z. Luo, Q. Yao, D. T. Leong, N. Yan and J. Xie, *Angew. Chem. Int. Ed.*, 2014, **53**, 4623–4627.
61 H. Qian, M. Y. Sfeir and R. Jin, *J. Phys. Chem. C*, 2010, **114**, 19935–19940.
62 M. S. Devadas, J. Kim, E. Sinn, D. Lee, T. Goodson and G. Ramakrishna, *J. Phys. Chem. C*, 2010, **114**, 22417–22423.
63 S. A. Miller, J. M. Womick, J. F. Parker, R. W. Murray and A. M. Moran, *J. Phys. Chem. C*, 2009, **113**, 9440–9444.
64 M. Zhu, C. M. Aikens, F. J. Hollander, G. C. Schatz and R. Jin, *J. Am. Chem. Soc.*, 2008, **130**, 5883–5885.
65 M. Greben, P. Khoroshyy, I. Sychugov and J. Valenta, *Appl. Spectrosc. Rev.*, 2019, **54**, 758–801.
66 V. W.-W. Yam and E. C.-C. Cheng, *Chem. Soc. Rev.*, 2008, **37**, 1806–1813.
67 P.-C. Chen, C.-K. Chiang and H.-T. Chang, *J. Nanoparticle Res.*, 2012, **15**, 1336.
68 T. Huang and R. W. Murray, *J. Phys. Chem. B*, 2001, **105**, 12498–12502.
69 J. R. Lakowicz, *Principles of Fluorescence Spectroscopy*, Springer, 2009.
70 K. G. Stamplecoskie and P. V. Kamat, *J. Am. Chem. Soc.*, 2014, **136**, 11093–11099.
71 S. H. Yau, O. Varnavski and T. Goodson, *Acc. Chem. Res.*, 2013, **46**, 1506–1516.
72 K. G. Stamplecoskie, Y.-S. Chen and P. V. Kamat, *J. Phys. Chem. C*, 2014, **118**, 1370–1376.

Nanoscale

CORRECTION

Cite this: DOI: 10.1039/d1nr90138a

Correction: Inverse heavy-atom effect in near infrared photoluminescent gold nanoclusters

Goutam Pramanik,[a] Klaudia Kvakova,[a] Muhammed Arshad Thottappali,[b,c] David Rais,[b] Jiri Pfleger,[b] Michael Greben,[c] Ayman El-Zoka,[d] Sara Bals,[d] Martin Dracinsky,[a] Jan Valenta*[c] and Petr Cigler*[a]

DOI: 10.1039/d1nr90138a
rsc.li/nanoscale

Correction for 'Inverse heavy-atom effect in near infrared photoluminescent gold nanoclusters' by Goutam Pramanik *et al.*, *Nanoscale*, 2021, DOI: 10.1039/d1nr02440j.

The authors regret that an incorrect version of Fig. 3 appeared in the original article. The correct Fig. 3, along with the accompanying caption, is as shown below:

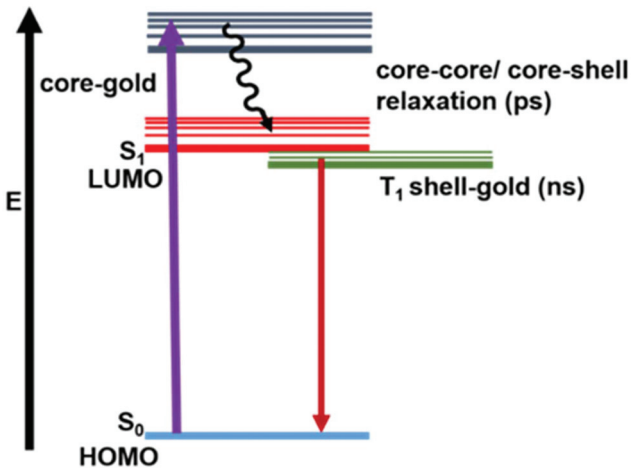

Fig. 3 Proposed scheme of photoexcitation and relaxation pathways of NIR PL AuNCs.

The Royal Society of Chemistry apologises for these errors and any consequent inconvenience to authors and readers.

[a]*Institute of Organic Chemistry and Biochemistry of the CAS, Flemingovo nam. 2, 166 10 Prague 6, Czechia. E-mail: cigler@uochb.cas.cz*
[b]*Institute of Macromolecular Chemistry of the CAS, Heyrovsky Sq. 2, 162 06 Prague 6, Czechia*
[c]*Faculty of Mathematics and Physics, Charles University, Ke Karlovu 3, 121 16 Prague 2, Czechia. E-mail: jan.valenta@mff.cuni.cz*
[d]*EMAT, University of Antwerp, Groenenborgerlaan 171, B-2020 Antwerp, Belgium*

Electronic Supplementary Information

Inverse Heavy-Atom Effect in Near Infrared Photoluminescent Gold Nanoclusters

Goutam Pramanik, Klaudia Kvakova, Muhammed Arshad Thottappali, David Rais, Jiri Pfleger, Michael Greben, Ayman El-Zoka, Sara Bals, Martin Dracinsky, Jan Valenta*, and Petr Cigler*

Corresponding authors: P. Cigler (cigler@uochb.cas.cz), J. Valenta (jan.valenta@mff.cuni.cz)

Materials

All reagents were purchased from commercial sources and used as received. Aqueous solutions for all experiments were prepared using Milli-Q water.

Synthesis of AuNCs

Synthesis of 1

AuNC **1** was prepared by following our previously reported procedure.[1] Briefly, thioctic acid (1.3 mg, 6.3 μmol) was dissolved in 3.9 mL MilliQ water by adding 10 μL of 2 M NaOH. After 15 min of stirring, 1.7 μL of $HAuCl_4.3H_2O$ (470 mg/mL) was added. The reaction mixture was stirred at room temperature for an additional 15 min, 80 μL freshly prepared $NaBH_4$ solution (1.9 mg/mL) was added, and the reaction mixture was stirred overnight. The next day, the solution was purified by three cycles of centrifugation/filtration using a membrane filtration device with a molecular weight cut-off (MWCO) of 3 kDa. Then, thiol-terminated polyethylene glycol (MW 2000; 2.6 mg; 1.3 μmol) was added to the solution and the pH was adjusted to 7-7.5. The mixture was stirred overnight. The dispersion was purified by three cycles of centrifugation/filtration using a membrane filtration device with MWCO of 3 kDa.

Synthesis of 2

A solution of **1** (4 mL, 0.2 mg/mL) and benzylamine (BA) (2 μL, ~18.3 μmol) was prepared, and the pH was adjusted to the 4.5 – 6.0 range with 1 M HCl. The mixture was stirred for 15 min. Then, the reaction was initiated by adding excess *N*-(3-dimethylaminopropyl)-*N*′-ethylcarbodiimide hydrochloride (EDC.HCl) (10 mg, 52 μmol) and stirred overnight. The following day, the dispersion was purified by three cycles of centrifugation/filtration using a membrane filtration device with a MWCO of 3 kDa to obtain **2**.

Synthesis of 3

4-Iodobenzylamine.HCl (iBA) (9.8 mg, ~ 36.6 μmol) was added to a solution of **1** (4 mL, 0.2 mg/mL), and the pH was adjusted to the 4.5 – 6.0 range with 1 M HCl. The mixture was stirred until iBA completely dissolved (~20-30 min). The reaction was started by adding excess EDC.HCl (10 mg, 52 μmol) and was stirred for 2 h. After 2 h, the pH of the reaction mixture was adjusted to 4.5 – 6.0 with 1 M HCl and an additional 10 mg EDC.HCl was added. The addition of EDC.HCl was repeated once more after 2 h, and the reaction mixture was stirred overnight at room temperature. Excess iBA and EDC.HCl were added thrice because of the slow reactivity of iBA with **1** compared with BA. The dispersion was purified by three cycles of centrifugation/filtration using a membrane filtration device with a MWCO of 3 kDa to obtain **3**.

Characterization of AuNCs

Elemental Analysis

Au, S, and N content were estimated using an optical emission spectrometer (OES) with radial observation of inductively coupled plasma (ICP) (SPECTRO Arcos – SPECTRO Analytical Instruments, Kleve,

Germany). The determination of N in solid AuNC samples was performed using an automatic PE 2400 Series II CHNS/O Analyser.

Table S1: Combined data from inductively coupled plasma optical emission spectrometry (ICP-OES) and CHN analysis.

Sample Name	Au (weight %)	S (weight %)	N (weight %)	Au (mol %)	S (mol %)	N (mol %)	Au/S molar ratio	Au/N molar ratio
2	21.34	4.44	0.32	0.10	0.13	0.023	0.76	4.34
3	16.12	3.6	0.26	0.08	0.11	0.019	0.72	4.21

NMR Measurements

NMR spectra were measured on a Bruker Avance III 500 spectrometer (499.88 MHz for ^{1}H) equipped with a 5 mm PFG cryoprobe. All ^{1}H spectra were acquired for samples in D_2O and referenced to the solvent signal (4.8 ppm).

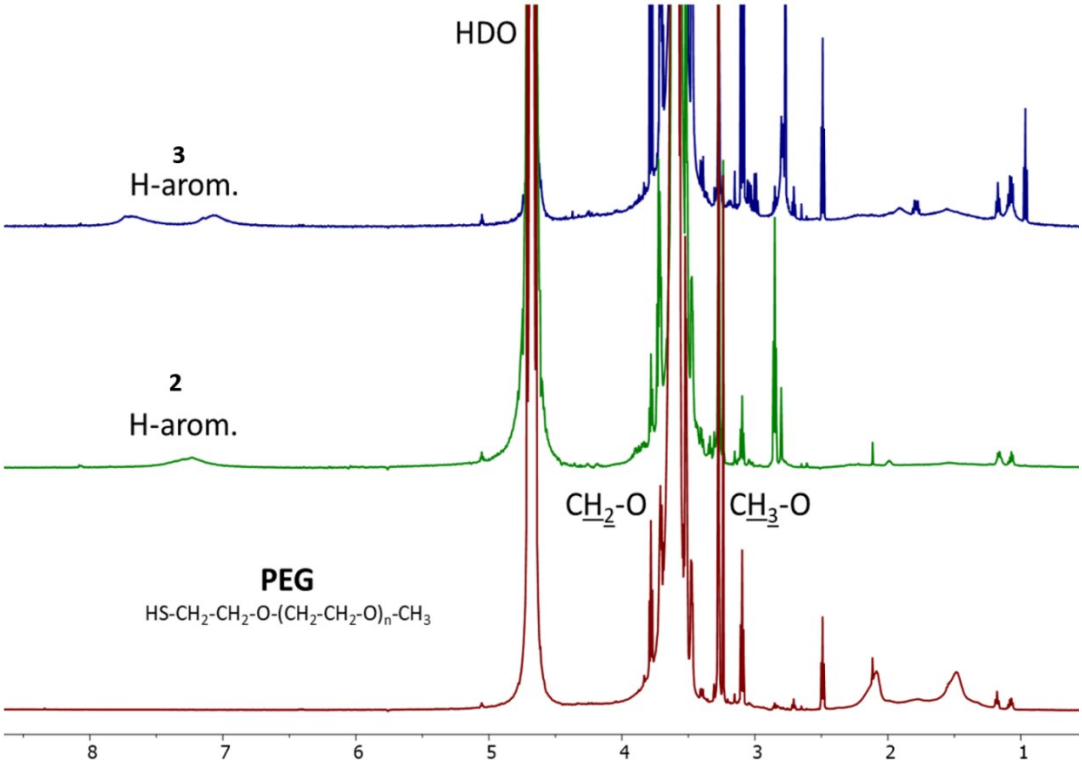

Figure S1: ^{1}H NMR (499.98 MHz, D_2O) of AuNC **2**, **3** and PEG. The peaks were referenced to the solvent signal.

Zeta potential measurements

Zeta potential experiments were carried out on a Zetasizer Nano ZSP (Malvern Instruments, Malvern, UK) with a 633 nm laser at 25 °C. Universal dip cells in disposable cuvettes were used. A 10-µL aliquot of AuNC solution (200 µg/mL) was mixed with 1 mL phosphate buffer solution (10 mM, pH 7.4) for measurement. Average values of at least three data points are reported.

High-resolution scanning transmission electron microscopy (HR-STEM) and X-ray photoelectron spectroscopy (XPS) measurements

The sizes of the AuNCs were determined by HR-STEM using an FEI Titan microscope. Samples were analyzed at a high voltage of 200 kV and a probe current of 50 pA.

XPS were measured using Omicron Nanotechnology equipment. The primary X-ray beam was monochrome radiation from an Al lamp with an energy of 1486.7 eV. The constant analyzer energy (CAE) mode was used, and the intensity calibration was based on copper and copper spectra-derived calibration constants. The ion gun used argon ions with an energy of ~5 keV; ion etching was carried out in the preparation chamber. A circular area with a diameter of approximately 0.8 mm was analyzed. The spectra were evaluated with CasaXPS software. The binding energy of a C 1s (284.8 eV) was used to calibrate the binding energy axis.

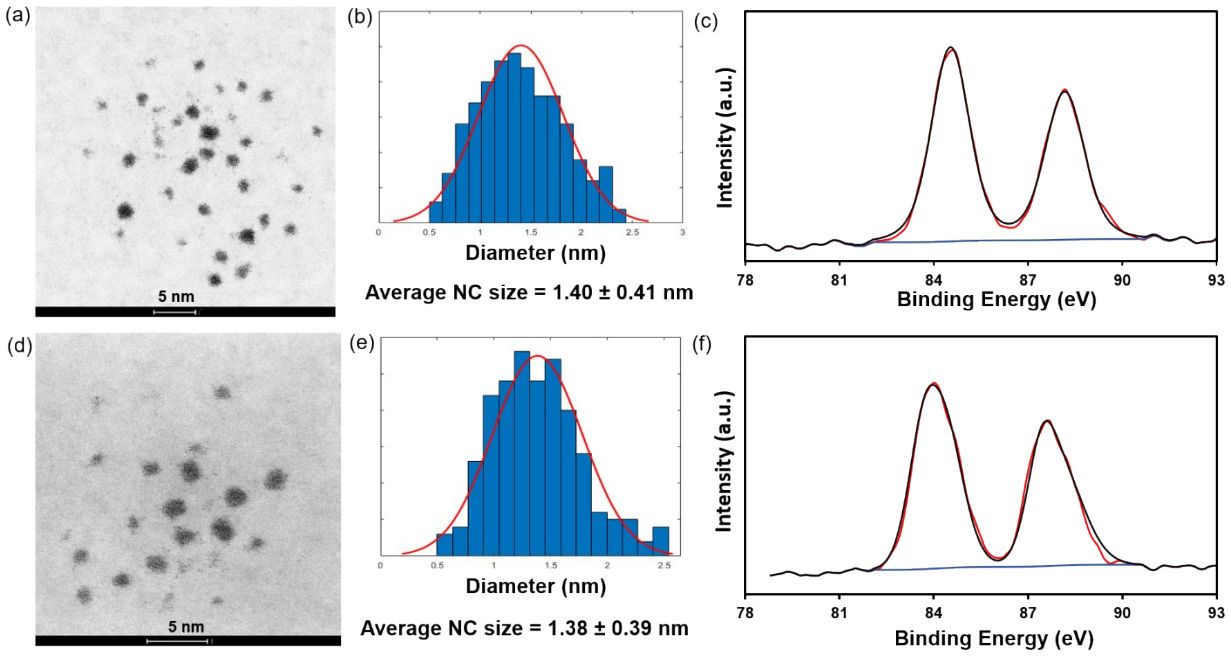

Figure S2: HR-STEM images of **2 (a)** and **3 (d)**. Particle size analysis of **2 (b)** and **3 (e)**. Particle size analysis of 200 AuNCs was performed for all samples. AuNCs were selected randomly from over 20 different locations in each sample. XPS spectra of the Au 4f peaks of **2 (c)** and **3 (f)**. The curves show that both AuNCs comprise Au(0) and Au(I).

UV-vis absorption and photoluminescence spectra, kinetics and yield measurements

UV-vis absorption spectra of aqueous solutions of AuNCs were measured with a Specord 250 spectrophotometer (Analytik Jena, Germany). Photoluminescence (PL) spectra were recorded under excitation by a cw 405-nm diode laser (MSL-III-405, CNI Co. Ltd., China) with acousto-optical modulation for time-resolved measurements and detected by an imaging spectrograph (SP 2300i, Acton, USA) with an LN-cooled CCD (Spec-10:400B, Princeton Instruments, USA) or (for time-resolved PL) a photon-counting photomultiplier (H11526–20-NF Hamamatsu, Japan) and multichannel scaler card (MSA-300, Becker & Hickl MSA-300, Germany).

As the excitation pulse sharpness (leading and trailing edges) produced by the AO modulator is approximately 100 ns, faster processes are not probed within these measurements, which can slightly affect the determined average decay time. However, in the case of significant presence of such processes, there should be an observable step down of PL signal at the end of the excitation pulse, which was not the case with our AuNCs.

PL decay kinetics were analyzed by three-exponential fitting:

$$I(t) = \sum_{i=1}^{3} A_i e^{-(\frac{t}{\tau_i})} + offset \qquad (1)$$

The PL quantum yield (Fig. S3) was measured with the same detection system (spectrometer and CCD) but excitation was performed using a laser-driven light source (LDLS, Energetiq, USA) coupled to a monochromator (SP 2150i, Acton, USA). Each sample was placed in a 10-cm diameter integrating sphere (Sphere Optics, Germany) with excitation and emission signals coupled via quartz fiber bundles (Newport, USA).

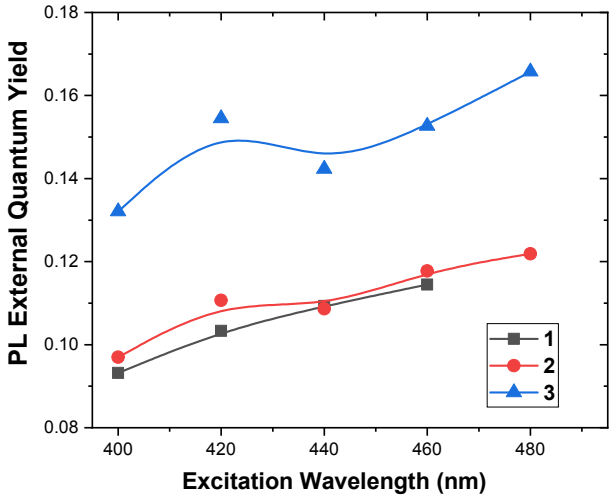

Figure S3: The external quantum yield of PL for excitation in the violet-blue-green spectral region. The PL QY uncertainty is about ±1%. The slight decrease of PL QY for excitation at short wavelengths may be due to increasing loses by absorption in ligands.

Transient Absorption measurements

Femtosecond transient absorption (fsTA) spectra were measured with ultrafast pump-probe experimental setup HELIOS (Ultrafast Systems, LLC, USA) using ultrafast laser source LEGEND ELITE (Coherent, USA) at 1 kHz repetition rate. The excitation pulses from TOPAS (Light Conversion, Lithuania) were adjusted to 360 nm and 260 nJ/pulse. The white-light continuum probe pulses were derived from the CaF_2 crystal. Laser pulses of both pump and probe beams were linearly polarized with mutual orientation of polarization at 55 deg. (magic angle) to suppress the rotational depolarization effect on the observed time evolution of the fsTA signal.

To observe the evolution of the transient absorption at the time scale longer than 6 ns (nsTA), the same source of probe light pulses was used as described above for fsTA. The pump pulses (wavelength 355 nm) were sourced from an electronically synchronized Nd-YAG laser (Surelite SL I-10, Continuum, USA) at the repetition rate 10 Hz, and frequency doubled using second harmonic generator and dichroic separator. The polarizations of the pump and probe pulses were also at the magic angle, as in the case of the fsTA.

TA spectra were measured with the sample colloids filled in 2 mm optical path quartz cuvettes under continuous stirring. For better understanding of the influence of atmospheric gases, the nsTA experiment was performed also with degassed samples in 10 mm optical path cuvettes equipped with a gas-tight valve.

Data analysis: Transient absorption datasets (both fsTA shown in Figure **S4** and nsTA in Figure **S5**) were analyzed using a global fitting approach. The spectro-temporal evolutions in femtosecond and picosecond time scale were well fitted with a sequential two-compartment kinetic model. The corresponding spectral profiles associated with the corresponding two-time constants sufficiently well fitted the observed transient spectra obtained from fsTA. However, since the lifetimes obtained from the fsTA experiment for the long-lifetime component markedly exceeded the maximum available delay time, we consider them not reliable and, hence, the long lifetimes shown in the main text of the paper were taken only from the nsTA experiment. Using global analysis, the data from the nsTA were relatively well fitted already with a single exponential kinetic model. Some wavelengths were, however, overestimated which lead to a sub-optimal fit for the wavelengths where the TA signal is more pronounced. Better agreement with experimental data was obtained when an additional component was added, with its life time much exceeding the experimental time scale (see table S2). For the sake of noise reduction, all spectral profiles shown in Fig. S5 were smoothed by adjacent averaging of 4-5 points.
In fsTA, no difference in the behavior of aerated and degassed colloids was observed. On the contrary, in longer delay times the difference was large, as seen from data obtained using nsTA (cf. Fig. S5c and S5d).

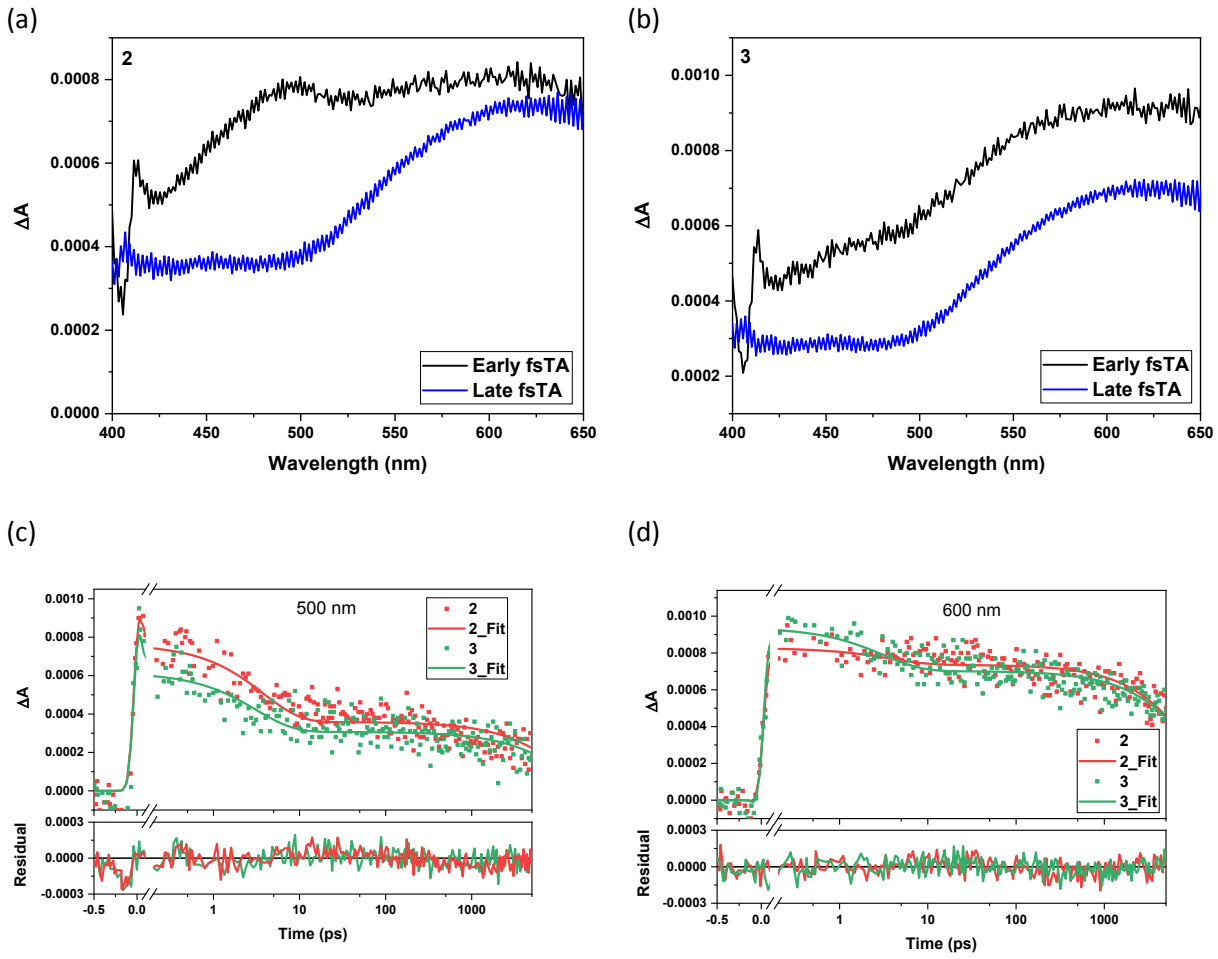

Figure S4: **a, b** – Short (black curves) and long (blue curves) transient absorption spectral components of colloids **2 (a)** and **3 (b)** as obtained from the global analysis of the fsTA measurements. **c, d** - temporal TA profiles obtained for probe wavelengths 500 nm **(c)** and 600 nm **(d)**, respectively. Excitation wavelength 360 nm in all cases. All colloids were aerated but no difference for the degassed colloids was observed.

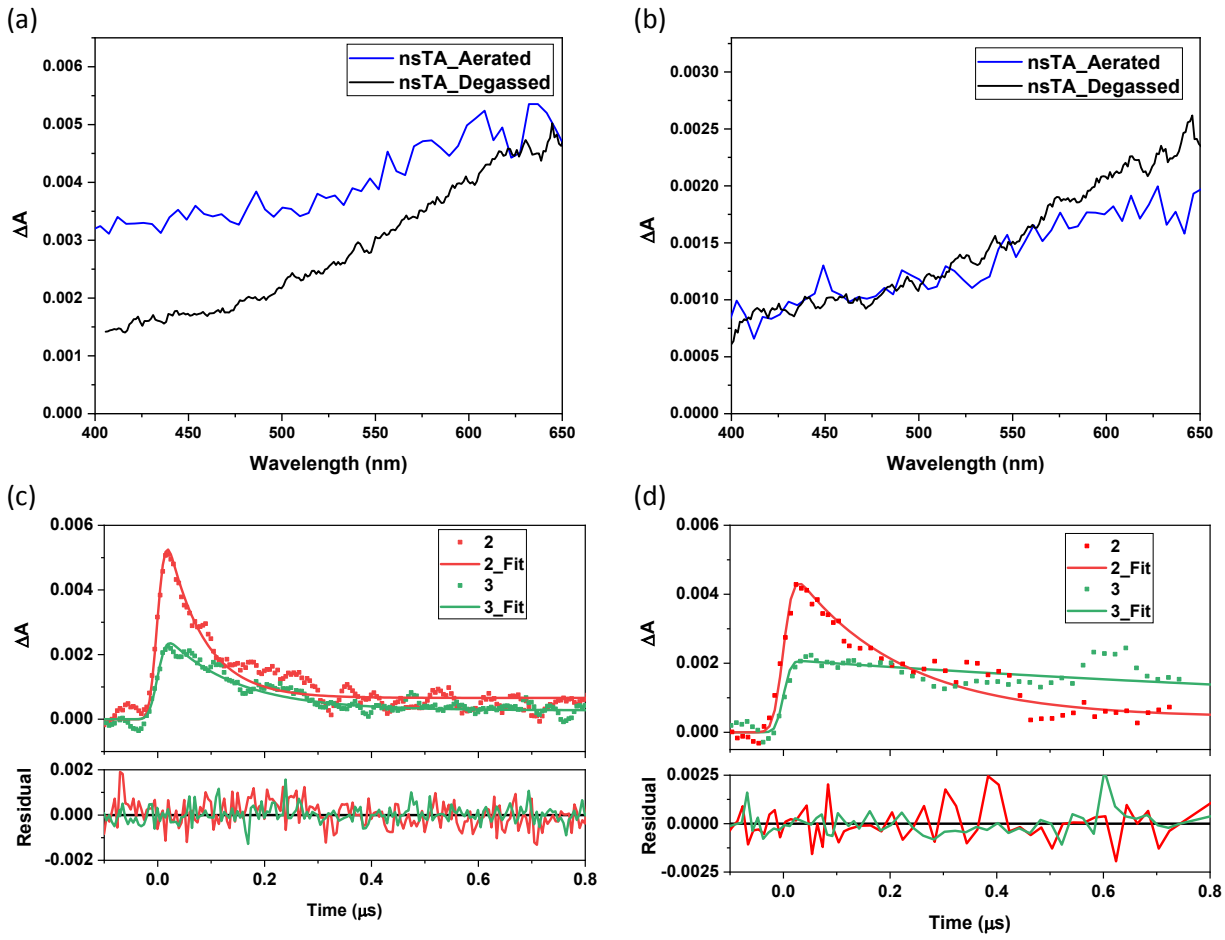

Figure S5: a, b - Transient absorption spectral components of aerated (blue curves) and degassed (black curves) colloids of samples **2 (a)** and **3 (b)**. **c, d** - kinetics of TA at the probe wavelength 600 nm measured with nsTA on aerated **(c)** and degassed **(d)** colloids of samples **2** (red) and **3** (green). Smooth curves show the fitted spectral and temporal profiles obtained from the global analysis. Excitation wavelength 355 nm in all cases.

Table S2: Lifetimes derived from individual spectral components.

Sample	fsTA	nsTA aerated					nsTA degassed				
		single exponential		bi-exponential kinetic model			single exponential		bi-exponential kinetic model		
	τ_1^{TA} (ps)	τ_2^{TA} (µs)	RMS value	τ_2^{TA} (µs)	τ_3^{TA} (µs)	RMS value	τ_2^{TA} (µs)	RMS value	τ_2^{TA} (µs)	τ_3^{TA} (µs)	RMS value
2	3.78 ± 0.01	0.16 ± 0.01	0.00093	0.07 ± 0.01	>> 10	0.00086	0.39 ± 0.01	0.00095	0.28 ± 0.01	140 ± 16	0.00087
3	3.16 ± 0.07	0.34 ± 0.01	0.00060	0.13 ± 0.01	>> 10	0.00055	2.12 ± 0.03	0.00069	1.86 ± 0.03	>> 10	0.00067

*) Lifetimes τ >> 10 µs are out of the time scale of nsTA experiment and could not be reliably determined. The RMS value as reported by Glotaran is the sum of squares of the errors divided by the number of degrees of freedom.

References:

1 G. Pramanik, J. Humpolickova, J. Valenta, P. Kundu, S. Bals, P. Bour, M. Dracinsky and P. Cigler, *Nanoscale*, 2018, **10**, 3792–3798.